KeAi
CHINESE ROOTS
GLOBAL IMPACT

Available online at www.keaipublishing.com/en/journals/journal-of-magnesium-and-alloys/

ScienceDirect

Journal of Magnesium and Alloys 12 (2024) 4966–4975

www.elsevier.com/locate/jma

Full Length Article

Layered double hydroxide-derived $Mg_2Ni/TiH_{1.5}$ composite catalysts for enhancing hydrogen storage performance of MgH_2

Gang Huang[a], Yao Lu[a], Xiaofang Liu[a,*], Wukui Tang[a], Xinyu Li[a], Feng Wang[a,b], Jianglan Shui[a,*], Ronghai Yu[a,*]

[a] *School of Materials Science and Engineering, Beihang University, No.37 Xueyuan Road, Beijing 100191, PR China*
[b] *School of Materials Science and Engineering & Guangxi Key Laboratory of Information Materials, Guilin University of Electronic Technology, Guilin 541004, PR China*

Received 7 August 2023; received in revised form 18 October 2023; accepted 26 October 2023
Available online 1 December 2023

Abstract

Developing efficient catalysts is of great significance in improving the sluggish kinetics and high desorption temperature of MgH_2 hydrogen storage material. Here, ultrathin NiTi-layered double hydroxide (NiTi-LDH) nanosheets are used as precursors to prepare $Mg_2Ni/TiH_{1.5}$ composite catalysts to improve the hydrogen storage properties of MgH_2. The variation of Ni/Ti ratio in LDH plays an important role in regulating the composition, morphology and distribution of $Mg_2Ni/TiH_{1.5}$ catalysts, which significantly affect their synergistic catalytic effect. $Mg_2Ni/TiH_{1.5}$ composite catalyst exhibits significantly improved catalytic performance compared with conventional Ni-, Ti- and Ni/Ti-based catalysts. The optimal $MgH_2/Mg_2Ni/TiH_{1.5}$ system shows a significantly reduced desorption temperature of 212 °C which is 133 °C lower than that of pure MgH_2 (345 °C), and can release 5.97 wt% hydrogen within 300s at 300 °C. Further mechanism analysis reveals that the unique flaky morphology and suitable composition of Ni/Ti LDH can significantly enhance the synergistic effect of Mg_2Ni and $TiH_{1.5}$, which promotes the fracture of the H–H and Mg-H bonds.

Keywords: Hydrogen storage materials; MgH_2; Layered double hydroxides; Nanocatalysts.

1. Introduction

Hydrogen is an ideal energy carrier because of its high chemical energy, environmental friendliness and renewability [1,2]. In order to achieve safe, efficient and compact hydrogen storage, various solid-state hydrogen storage materials, such as metal hydrides [3–5], complex hydrides [6–8], carbon materials [9,10], metal-organic frameworks (MOFs) [11–14], MXene [15], have been developed over the past decades based on the physisorption or chemisorption of hydrogen [16]. Magnesium hydride is an attractive candidate for solid-state hydrogen storage applications due to its high hydrogen storage density (mass capacity of 7.6 wt% H_2 and volumetric capacity of 111 $kg{\cdot}m^{-3}$) [17], superior thermal conductivity [18], low density and abundance of Mg element on the Earth. However, the sluggish kinetics and high thermodynamic stability of MgH_2 (ΔH=74.5 $kJ{\cdot}mol^{-1}$) result in its high operation temperature and low hydrogen sorption rate. Nowadays, a variety of strategies have been developed to solve these issues by tuning the thermodynamics and kinetics of magnesium hydride [19–21], including nano-crystallization [22–24], alloying [25,26], catalyst doping [27–32], advanced processing technologies [33–35], and so on.

Among these methods, catalyst doping is a common and effective method to improve the hydrogen storage kinetic properties of MgH_2. So far, many kinds of catalysts have been used to accelerate the diffusion of hydrogen and destabilize the Mg-H bond in the Mg/MgH_2 system [36–47]. Especially, Ti and its compounds exhibit good catalytic effects and aroused widespread interests. For example, Cui et al. [38]

* Corresponding authors.
E-mail addresses: liuxf05@buaa.edu.cn (X. Liu), shuijianglan@buaa.edu.cn (J. Shui), rhyu@buaa.edu.cn (R. Yu).

https://doi.org/10.1016/j.jma.2023.10.003

reported that due to the low electronegativity of Ti element, the Ti nanoparticles-coated Mg composite (Mg-Ti) can release 6.275 wt% of hydrogen within 600s at 275 °C, which is superior to other Mg-TM (TM: Ti, Nb, V, Co, Mo or Ni) composites. Wang et al. [48] studied the catalytic effects of different Ti-based materials (Ti, TiF_3, TiO_2, TiN) on the dehydrogenation performances of MgH_2. It is found that these catalysts underwent different reaction processes and transformed into different active species during the dehydrogenation. TiF_3 showed the best catalytic effect due to the formation of active TiH_x. Compared to single-component catalysts, composite catalysts have received increasing attention because the synergistic effects of different components are beneficial for improving catalytic performance. For example, MgH_2 with Ni/TiO_2 composite catalysts could desorb several times higher hydrogen than MgH_2 with single Ni catalyst or single TiO_2 catalyst [49]. Similarly, the catalytic efficiency of $SrTiO_3$/Ni composite catalysts for MgH_2 is higher than that of single $SrTiO_3$ or Ni catalyst [50]. Moreover, the morphology of catalyst also plays an important role in regulating catalytic effects. Many 1D and 2D catalysts such as porous Ni nanofibers [51], $Na_2Ti_3O_7$ nanotubes [52] and flower-like TiO_2@C [44] exhibit enhanced catalytic effects on the hydrogen storage performance of MgH_2. Therefore, to design an efficient composite catalyst, it is necessary to comprehensively consider multiple factors, such as the selection and proportion of various components, their morphology and distribution. Exploring the mechanisms of these complex factors on the catalytic performances is currently a hot and challenging task.

Recently, layered double hydroxides (LDHs), a family of 2D layered clays, have been widely studied in photocatalysis, solar cells, CO_2 adsorbents and functional materials [53–55]. Its tunable composition and morphology provide enormous potential for designing abundant oxide and metal composite materials, thus inspiring us to use it as a precursor to prepare efficient catalysts for Mg/MgH_2 system. In this work, we prepared ultrathin NiTi-LDH nanosheets, and calcined them into NiO-TiO_2 composite through a topotactic transformation. By adjusting the Ni/Ti ratio, various mixed metal oxides (MMO) with morphologies from nanosheets to nanoparticles and multiple crystal phases were successfully obtained. These MMO nanosheets were in-situ converted to Mg_2Ni-$TiH_{1.5}$ composite catalysts on MgH_2 particles during activation process. Benefitting from the synergistic effect of Mg_2Ni and $TiH_{1.5}$, the MgH_2 decorated with this composite catalyst exhibits much better hydrogen storage performances than the MgH_2 decorated with a single Ni- or Ti-based catalysts. Moreover, the unique morphology and composition of NiTi-LDH precursors endow the resultant composite catalyst with superior catalytic ability to conventional Ni/Ti composite catalysts derived from a mixture of NiO and TiO_2. The optimal MgH_2/Mg_2Ni/$TiH_{1.5}$ system shows a considerably reduced desorption temperature of 212 °C, and can release 5.97 wt% hydrogen within 300s at 300 °C. Finally, the mechanism of the enhanced catalytic efficiency is revealed from the aspects of catalyst composition, morphology and distribution.

2. Experimental

2.1. Synthesis of Ni/Ti precursor

Ni/Ti precursors were prepared by a coprecipitation method according to the previous literature [56]. Typically, 0.001mol $TiCl_4$ (dissolved in HCl solution with a volume ratio of 1:1), $Ni(NO_3)_2{\cdot}6H_2O$ (0.004mol), and urea (0.05mol) were dissolved in deionized water (50mL) under vigorously stirring at refluxing temperature (110 °C) for 27h. The precipitation was centrifuged, washed thoroughly and dried at 60 °C. According to the molar ratio of Ni^{2+}/Ti^{4+}, the obtained powder sample was denoted as precursor41. Samples with a molar ratio of Ni^{2+}/Ti^{4+} of 1:4, 1:2, 2:1 and 6:1 were prepared using the same method, and the corresponding samples were denoted as precursor14, precursor12, precursor21 and precursor61.

2.2. Synthesis of Ni/Ti MMO

Ni/Ti MMO were prepared by calcining the above Ni/Ti precursors in a mixture of oxygen (40 ml·min^{-1}) and argon (60 ml·min^{-1}) at 500 °C for 2h. The obtained MMO was denoted as MMO14, MMO12, MMO21, MMO41 and MMO61. For comparison, pure NiO and TiO_2 were also synthesized using the same method.

2.3. Synthesis of Ni/Ti MMO-MgH_2 composite

The as-prepared Ni/Ti MMO with different composition was mixed with MgH_2 (Seri Beida Technology Co., Ltd., particle size<10μm, 98%). Fig. S1 shows the morphology and crystal structure of the raw MgH_2. Then the mixture was mechanically ball milling under 1.2bar Ar for 6h with a milling speed of 400rpm. The mass fraction of Ni/Ti MMO in composite was 5%. The ball-to-powder ratio was 40:1. In addition, pure MgH_2 was milled under the same conditions without any extra additives. All the sample were stored in a glove box filled with Ar to prevent oxidation.

2.4. Characterization

The phase composition of the products was characterized using X-ray diffraction (Rigaku) with Cu-Kα radiation (40kV and 200mA). The morphology and microstructure of the products were observed by scanning electron microscopy (SEM, JEOL JSM-7500) and transmission electron microscope (TEM, JEOL JSM-2200FS) equipped with energy dispersive X-ray spectrometer.

The measurement of the hydrogen storage properties of the MgH_2–Ni/Ti-MMO composites were performed on a homemade Sieverts-type pressure-composition-temperature (PCT) volumetric apparatus. 0.2 g of the composite was loaded into a stainless-steel sample chamber in a glovebox filled with argon. Before hydrogen storage performance test, the samples were activated as follows: (1) The samples were heated to 400 °C and then vacuumed for 0.5h. (2) The samples were

Table 1
Summary of morphology, phase and grain size of MMO catalyst.

	MMO61	MMO41	MMO21	MMO12	MMO14
Morphology	nanosheets	nanosheets	aggregated nanoparticles	aggregated nanoparticles	aggregated nanoparticles
Phase	anatase TiO_2, NiO	anatase TiO_2, NiO	anatase TiO_2, NiO	anatase TiO_2, brookite TiO_2, NiO	anatase TiO_2, brookite TiO_2, NiO
Grain size/nm	8.2	5.2	6.4	5.2	5.5

exposed to hydrogen under a pressure of 2MPa until saturation at a temperature of 200 °C. (3) The samples were heated to 350 °C for dehydrogenation in vacuum. The temperature programmed desorption (TPD) profiles were tested from room temperature to 400 °C with a heating rate of 5 °C·min^{-1}. The absorption and desorption kinetics measurements were performed using an initial hydrogen pressure of 2 MPa for hydrogenation and 0.0001 MPa for dehydrogenation at 250, 275, and 300 °C, respectively. The as-prepared composite was completely dehydrogenated at 400 °C before the isothermal hydrogen sorption measurements. For dehydrogenation PCT measurement, the dehydrogenated sample was rehydrogenated to saturation under a hydrogen pressure of 2 MPa, heated to the target temperature at 5 °C·min^{-1}, and maintained at this temperature to measure PCT curves. During the cycling stability measurement, the samples were hydrogenated under a hydrogen pressure of 2 MPa, and desorbed hydrogen into a pre-evacuated reservoir (about 1L) at 300 °C.

3. Results and discussion

3.1. Structure and morphology characterizations of Ni/Ti-based catalysts

First, Ni/Ti precursors were prepared by co-precipitating Ni and Ti metal salts, as shown in Fig. 1(a). The Ni/Ti ratio in the precursor was adjusted from 6/1, 4/1, 2/1, 1/2, to 1/4 (denoted as precursor61, −41, −21, −12, −14). XRD characterization indicates that the Ni/Ti ratio has a significant effect on the crystal phase of the precursor (Fig. 1b, c, S2a). All the diffraction peaks in the XRD patterns of precursors61/41/21 with low Ti ratio belong to NiTi-LDH (JCPDS File No. 38–487). However, as the Ti ratio further increases, the phase of the precursors14/12 changes to a mixture of anatase and brookite. Besides, the morphology of the Ni/Ti precursors changes with the increase of Ti content. Precursors61/41 show sheet-like structures (Fig. 1c, d), while precursors21/12/14 are aggregates of nanoparticles (Fig. S2b–d). After heat treatment in air, the precursors61/41/21 were converted to a mixed metal oxides of NiO and TiO_2 (anatase) (denoted as MMO61, MMO41 and MMO21) (Figs. 1e and S3a). In contrast, MMO14 and MMO12 have no obvious phase transition and are still a mixture of anatase and brookite. MMO61 and MMO41 inherit the nanosheet morphologies of the precursors (Fig. 1f, g), and the lateral dimension of a single sheet is about 90nm. In contrast, MMO21/12/14 remain agglomeration of nanoparticles (Fig. S3b-d). The grain size of the MMO samples was calculated according to the Scherrer formula. As summarized in Table 1, the grain size is 8.2 nm for MMO61, 5.2 nm for MMO41, 6.4 nm for MMO21, 5.2 nm for MMO12 and 5.5 nm for MMO14. The obtained MMO samples were compounded with MgH_2 through ball milling (denoted as MgH_2−MMO), and ultimately converted into $Mg_2Ni/TiH_{1.5}$ composite catalysts in situ during the activation process.

3.2. Catalytic effect of MMO on the hydrogen storage performances of MgH_2

Before hydrogen storage performance tests, the as-milled MgH_2 and MgH_2–5%MMO samples were activated by hydriding/dehydriding once (Fig. S4). The catalytic effect of MMO on the dehydrogenation of MgH_2 was first investigated by temperature-programmed desorption (TPD) measurements. Figs. 2 and S5 show the TPD curves of ball-milled MgH_2 and a series of MgH_2–5%MMO (weight percentage of MMO: 5 wt%) composites. The onset dehydrogenation temperature of the as-milled MgH_2 is as high as 345 °C, and the dehydrogenation amount is ∼7.35 wt%, close to the theoretical hydrogen storage capacity. The addition of MMO catalysts lowers the dehydrogenation temperature. The Ni/Ti ratio affects the catalytic effect of the MMO catalyst. The onset dehydrogenation temperatures of MgH_2–5%MMO41 and MgH_2–5%MMO12 are ∼210 °C while those of the other composite samples are ∼240 °C. Meanwhile, the dehydrogenation amount decreases to 6.39 wt% for MgH_2–5%MMO61, 6.45 wt% for MgH_2–5%MMO41, 6.20 wt% for MgH_2–5%MMO21, 6.40 wt% for MgH_2–5%MMO12 and 6.36 wt% for MgH_2–5%MMO14 due to the dead weight of the additives. To optimize the addition amount of catalyst, MgH_2 was mixed with different amounts of MMO41 (MgH_2-*x*%MMO41, *x*=3, 5 and 7 wt%) by ball milling and subjected to isothermal dehydrogenation tests at 250, 275, and 300 °C, respectively. With the increase of catalyst content, the dehydrogenation amount of MgH_2−MMO41 gradually decreases (Fig. S6). Among the three samples, the MgH_2–5%MMO41 composite shows the fastest dehydrogenation rate at each temperature.

To compare the dehydrogenation kinetics, isothermal dehydrogenation measurements were performed on as-milled MgH_2 and MgH_2–5%MMO at 300, 275 and 250 °C, respectively. The as-milled MgH_2 has sluggish dehydrogenation kinetics, and only released 1.40 wt% hydrogen within 50min at 300 °C (Fig. 3a). After incorporating catalysts, the composites show significantly improved dehydrogenation kinetics (Figs. 3b, c and S7). Comprehensively considering the dehy-

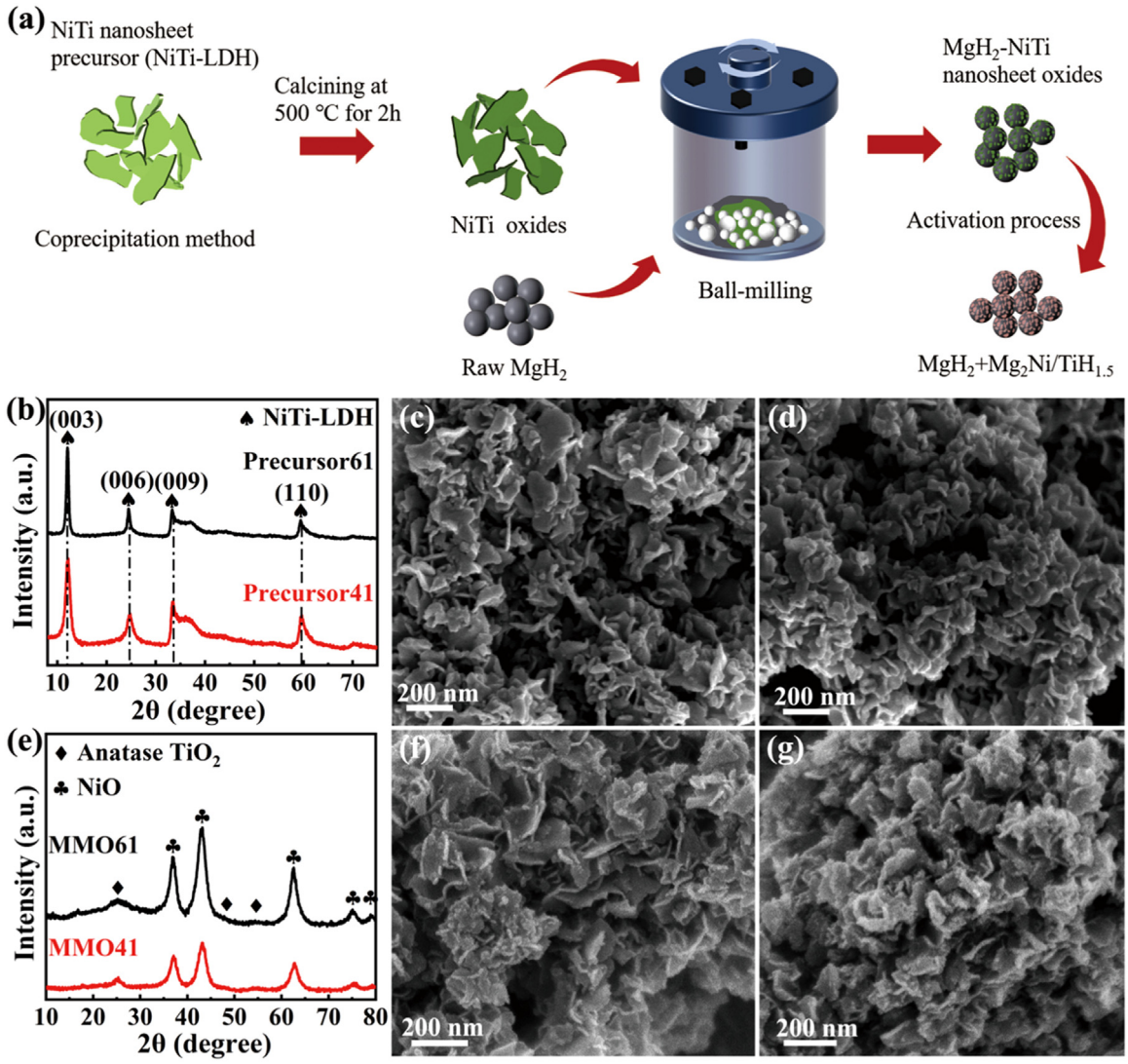

Fig. 1. (a) Schematic illustration of the preparation of MMO-MgH_2 composites. XRD patterns of (b) precursor61 and precursor41. SEM images of (c) precursor61, (d) precursor41. XRD patterns of (e) MMO61 and MMO41. SEM images of (f) MMO61, (g) MMO41.

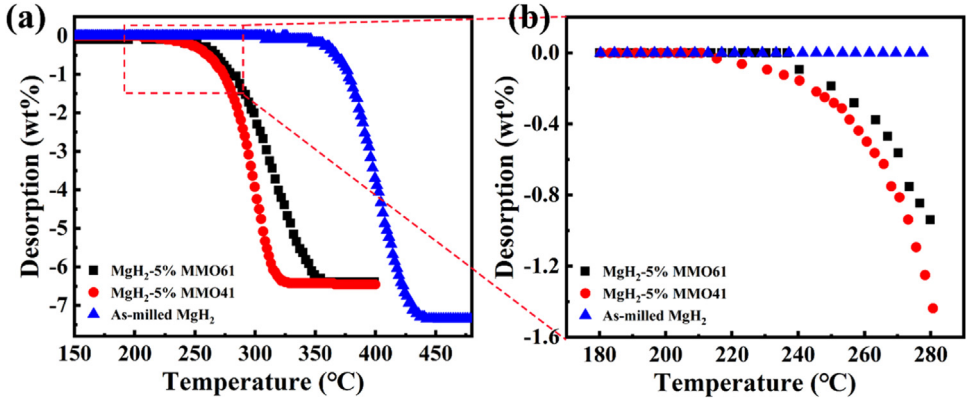

Fig. 2. TPD measurements of (a) as-milled MgH_2, MgH_2–5%MMO61 and MgH_2–5%MMO41, (b) an enlarged view from 180 to 280 °C. (heating rate: 5 °C·min^{-1}).

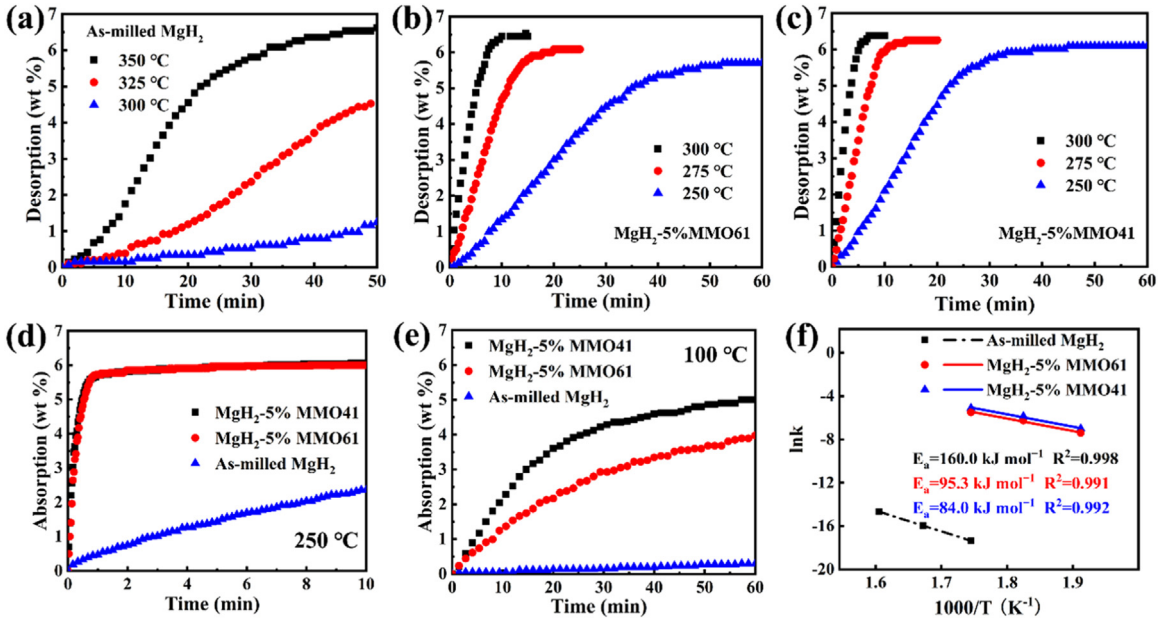

Fig. 3. Isothermal desorption curves of (a) as-milled MgH_2, (b) MgH_2–5%MMO61 and (c) MgH_2–5%MMO41 and their isothermal absorption curves at (d) 250 °C and (e) 100 °C, and (f) Arrhenius plots of dehydrogenation.

drogenation rate and the available hydrogen amount, MgH_2–5%MMO41 has the best dehydrogenation properties among the five composites. At 300 °C, the MgH_2–5%MMO41 released 5.97 wt% hydrogen within 5min. The corresponding average dehydrogenation rate was calculated to be 1.19 wt%·min^{-1}, which is about 20 times faster than that of MgH_2 (0.06 wt%·min^{-1}). When the dehydrogenation temperature decreased to 250 °C, the dehydrogenation amount of the MgH_2–5%MMO41 was 4.46 wt% in 20min. Subsequently, the dehydrogenated MgH_2 and MgH_2–5%MMO samples were rehydrogenated under 20bar hydrogen to evaluate the effect of MMO catalysts on hydrogen uptake at 250 and 100 °C (Figs. 3d, e and S8). Compared with the as-milled MgH_2, the hydrogen absorption performances of all MgH_2–5%MMO samples are considerably improved. At 250 °C, MgH_2–5%MMO61 and −41 performed the best, and the hydrogen absorption reached saturation within 60s.

To gain further insight into the dehydrogenation kinetics, the activation energy (E_a) of MgH_2–5%MMO was determined using the JMAK (Johnson-Mehl-Avrami-Kolmogorov) model (Eq. (3.1)).

$$ln(-ln(1-\alpha)) = \eta \cdot lnt + \eta \cdot lnk \tag{3.1}$$

where k is the reaction rate constant, η is the Avrami exponent of the reaction order, and α ($0.2 < \alpha < 0.7$) is the fraction transformed at time t. The plots of $\ln[-\ln(1-\alpha)]$ vs. $\ln(t)$ for the dehydrogenation of the MgH_2–5%MMO composites are straight lines, where η and $\eta\ln(k)$ represent the slope and intercept (Fig. S9a–e). The rate constant k for each temperature can be obtained and used to calculate the dehydrogenation E_a according to the Arrhenius equation:

$$k = A \cdot exp(E_a/RT) \tag{3.2}$$

The calculated E_a values of MgH_2–5%MMO composites are in the range of 84.0–107.9 kJ·mol^{-1} (Figs. 3f and S9f), lower than those of as-milled MgH_2 (160.0 kJ·mol^{-1}) and other Ni/Ti-doped MgH_2 systems, such as MgH_2–Ni/Ti_3C_2 (91.6 kJ·mol^{-1} [57]), MgH_2-$SrTiO_3$@Ni (98.6 kJ·mol^{-1} [50]), MgH_2–Ni_4@rGO_6 (117.8 kJ·mol^{-1} [58]), MgH_2–Ni (116 kJ·mol^{-1} [59]), MgH_2-$TiCl_3$ (97 kJ·mol^{-1} [60]) and MgH_2-TiH_2 (89.4 kJ·mol^{-1} [61]), which proves the reduction of dehydrogenation kinetic barrier of MgH_2 by MMO catalysts. The dehydrogenation rate, onset dehydrogenation temperature and dehydrogenation activation energy of MgH_2–5%MMO composites were summarized in Fig. 4(a) and Table S1, indicating that MMO41 has the best catalytic effect on MgH_2. Furthermore, we compared the hydrogen storage properties of MgH_2–5%MMO41 with other MgH_2 added with Ni/Ti-based catalysts (Table S2 and Fig. 4b). It is clear that the de/rehydrogenation kinetics of MgH_2–5%MMO41 are superior to most other composites.

3.3. Pressure-composition-isothermal measurements of the MgH_2–5wt%MMO-41

Fig. 5(a) presents the pressure-composition-temperature curves (PCT) of bulk MgH_2 and MgH_2–5%MMO41 at 300, 325 and 350 °C. The broad and flat plateau represents the phase transition between the metal hydride and its hydrogen released product. Based on these data, the enthalpy and entropy changes of the reaction can be calculated using Van't Hoff equation:

$$\ln P_{eq} = -\frac{\Delta H}{RT} + \frac{\Delta S}{R} \tag{3.3}$$

The plateau pressures of MgH_2–5%MMO41 at 350, 325, and 300 °C are 0.44, 0.24, and 0.13 MPa, respectively,

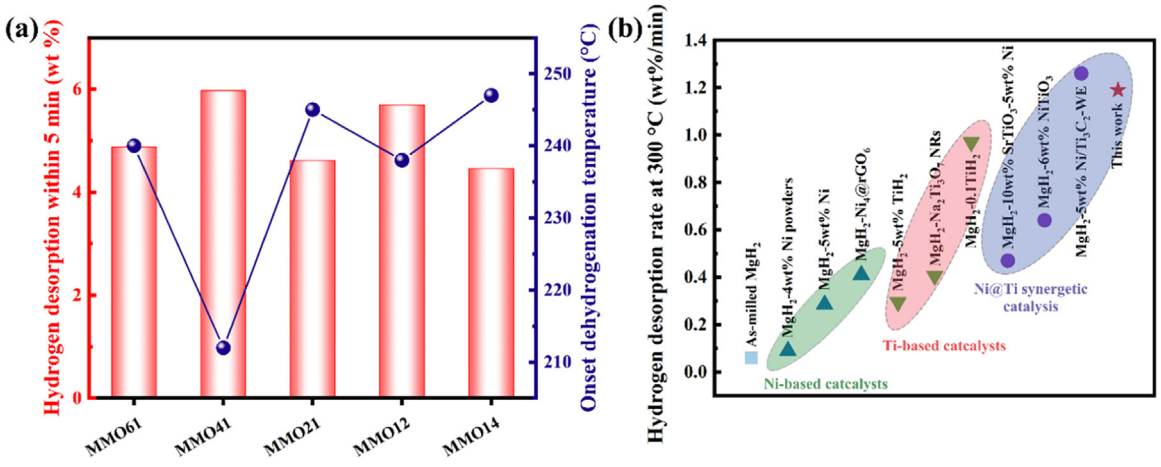

Fig. 4. (a) Comparison of dehydrogenation rate and onset dehydrogenation temperature of MgH_2–5%MMO composites. (b) Comparison of dehydrogenation rate (at 300 °C) of MgH_2 with Ni/Ti-based catalysts.

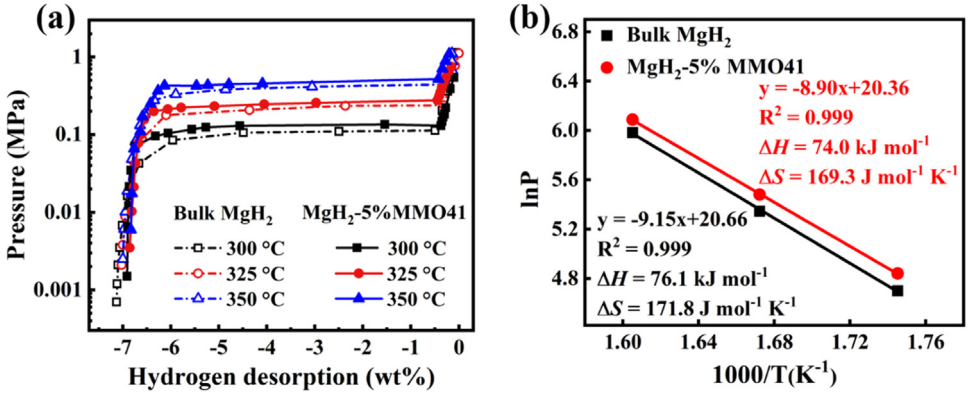

Fig. 5. (a) PCT curves of dehydrogenation of bulk MgH_2 and MgH_2–5%MMO41. (b) Corresponding Van't Hoff curve of bulk MgH_2 and MgH_2–5%MMO41.

while the plateau pressures of bulk MgH_2 are 0.39, 0.21, and 0.11MPa, respectively. By fitting the Van't Hoff plot in Fig. 5(b), the dehydrogenation enthalpy change (ΔH) and entropy change (ΔS) of MgH_2–5%MMO41 were calculated to be 74.0 kJ·mol^{-1} H_2 and 169.3 J·mol^{-1}·K^{-1} H_2, respectively, and these values of bulk MgH_2 are 76.1 kJ·mol^{-1} H_2 and 171.8 J·mol^{-1}·K^{-1} H_2, close to the results in literatures (74.7 kJ·mol^{-1} H_2 [62] and 133.9 J·mol^{-1}·K^{-1} H_2 [63]). It suggests the negligible effect of catalyst on dehydrogenation thermodynamics of MgH_2. For the MgH_2 dehydrogenation reaction system, the increase of entropy mainly comes from the increased entropy value of the released hydrogen [41].

3.4. The catalytic mechanism of MMO on hydrogen storage performance of MgH_2

It is well known that the kinetics of hydrogen storage in magnesium is mainly determined by two key processes: the dissociation of H_2 molecules and the diffusion of H atoms into the bulk [38]. The addition of catalysts can greatly promote the dissociation rate of H_2 molecules [41]. To clarify the catalytic mechanism of MMO, three control samples were prepared by ball milling MgH_2 with 5 wt% of NiO, TiO_2, and a mixture of NiO and TiO_2 (molar ratio of 4:1), respectively. Their isothermal dehydrogenation curves were measured at 300, 275 and 250 °C, as shown in Fig. 6(a–c). The dehydrogenation kinetic properties of the three control samples follow the order of MgH_2–5%NiO > MgH_2–5%(NiO+TiO_2) > MgH_2–5%TiO_2, but much worse than that of MgH_2–5%MMO. To further study the dehydrogenation kinetics, we calculated the E_a of MgH_2–5%NiO and MgH_2–5% (NiO + TiO_2), which are 102.6 and 95.6kJ mol^{-1}, respectively (Fig. 3f and Fig. 6f). The E_a of MgH_2–5%TiO_2 is not given because its low dehydrogenation capacity cannot guarantee sufficient calculation accuracy. The above comparison shows that the catalytic effect of MMO is not the superposition of NiO and TiO_2 components, but a synergistic effect of 1+1>2.

The catalytic performance of MMO is closely related to the Ni/Ti ratio and the MMO morphology. XRD characterization indicates that the initial MMO catalyst composed of NiO and TiO_2 phases was converted to Mg_2Ni and $TiH_{1.5}$ phases during activation process due to the reduction by hydrogen (Fig. 7a, Figs. S10 and S11). Therefore, the Ni/Ti ratio in precursor affects the ratio of Mg_2Ni to $TiH_{1.5}$ phases in the mixture. Mg_2Ni has a high hydrogen affinity and provides catalyst-matrix interface, which acts as a "hydrogen pump" to promote hydrogen diffusion [38,64]. TiH_x is an efficient cata-

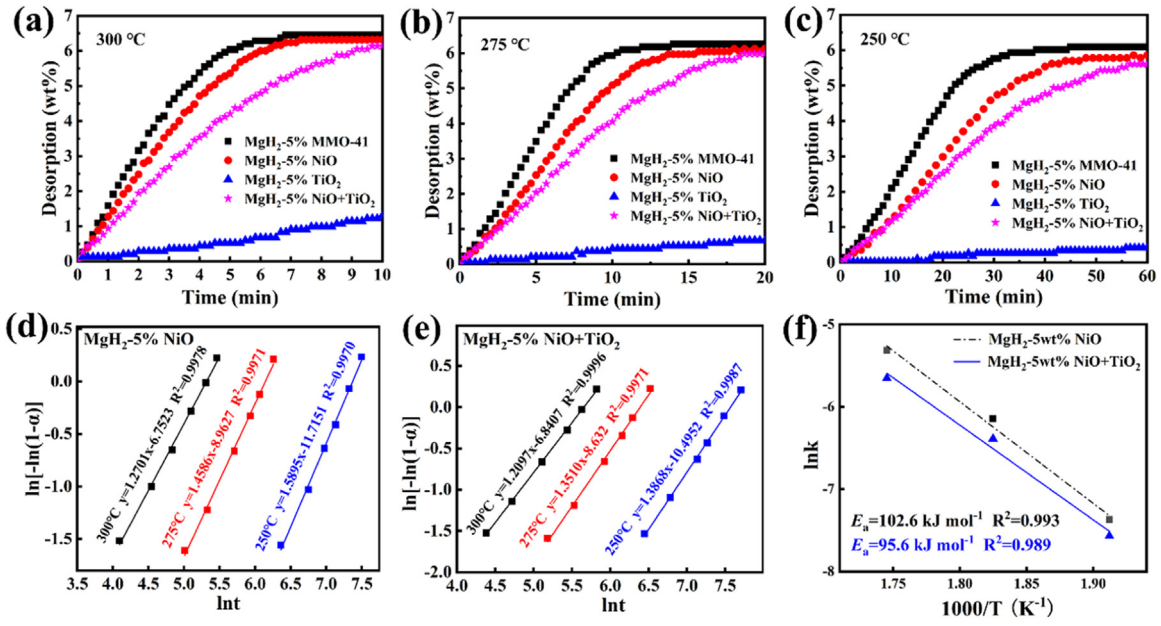

Fig. 6. Isothermal desorption curves of MgH_2 added with 5%MMO41, -NiO, -TiO_2 and NiO+TiO_2 at (a) 300 °C, (b)275 °C, (c) 250 °C. (d-e) JMAK plots of $\ln[-\ln(1-\alpha)]$ vs. $\ln(t)$ and (f) their Arrhenius plots.

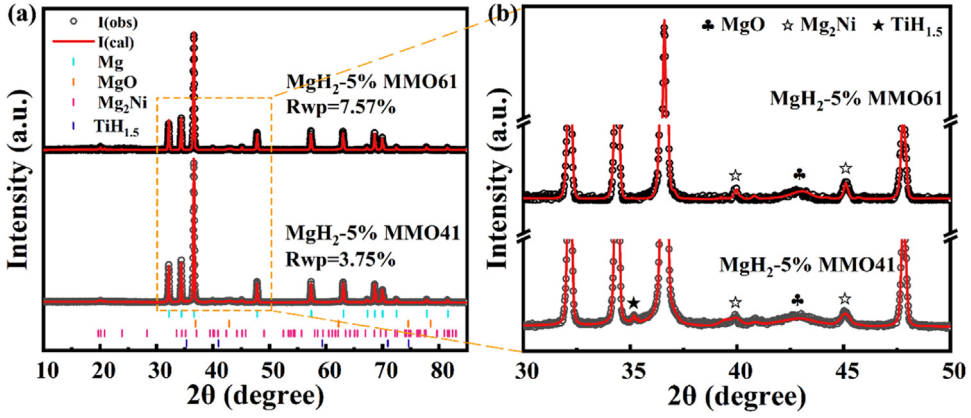

Fig. 7. (a) XRD patterns of MgH_2–5%MMO41 and MgH_2–5%MMO61 after dehydrogenation, (b) corresponding enlarged view.

lyst that can change the reaction thermodynamics of MgH_2 by weakening the Mg-H bond [65–67]. From the Rietveld refinement results of XRD patterns (Fig. 7) and Table S3, we can deduce that the MMOs with high Ni/Ti ratio (MMO61) and low Ni/Ti ratio (MMO14, Fig. S12) were converted to Mg_2Ni single phase and $TiH_{1.5}$ single phase, respectively, which fails to produce the synergy effect. The MMO with appropriate Ni/Ti ratio such as MMO41 was converted to a mixture of Mg_2Ni (3.7 wt%) and $TiH_{1.5}$ (0.8 wt%), which has better catalyst effect due to their synergistic effect. More importantly, the morphology of MMO41 after ball milling of MgH_2–5%MMO41 still keeps fine grains (Fig. S10). Additionally, since Ti^{4+} has more O coordination than Ni^{2+}, the MgO content in the composite increases as the ratio of Ni/Ti in precursor decreases. Although the catalyst composition in MgH_2–5% (NiO + TiO_2) is similar to that of MgH_2–5%MMO41, the kinetics of MgH_2–5% (NiO + TiO_2) is much worse, implying that the morphology of catalyst has a great influence on the catalytic performance. As shown in Fig. 1, Fig. 8 and Fig. S13, MMO41 catalyst has a sheet-like structure, while the single catalyst of NiO and TiO_2 or their mixtures exhibit agglomerated particles. Compared with agglomerated mixed particles, nanosheets are more uniformly distributed on the surface of MgH_2 particles during ball milling (Fig. 9). During the activation process, the Mg_2Ni and $TiH_{1.5}$ nanoparticles generated by MMO reduction have smaller size and more uniform distribution on MgH_2 particle surface, which is more conducive to generating synergistic effects. According to the above analysis, the catalytic mechanism of MMO in MgH_2 can be concluded as shown in Fig. 10.

3.5. The reversible cyclic hydrogen storage performance of MgH_2-MMO41

The reversible cyclic hydrogen storage performance is a key indicator for hydrogen storage materials. Fig. 11a shows the hydrogen storage performance of MgH_2−MMO41 during 20 cycles. The hydrogen absorption capacity decreased from

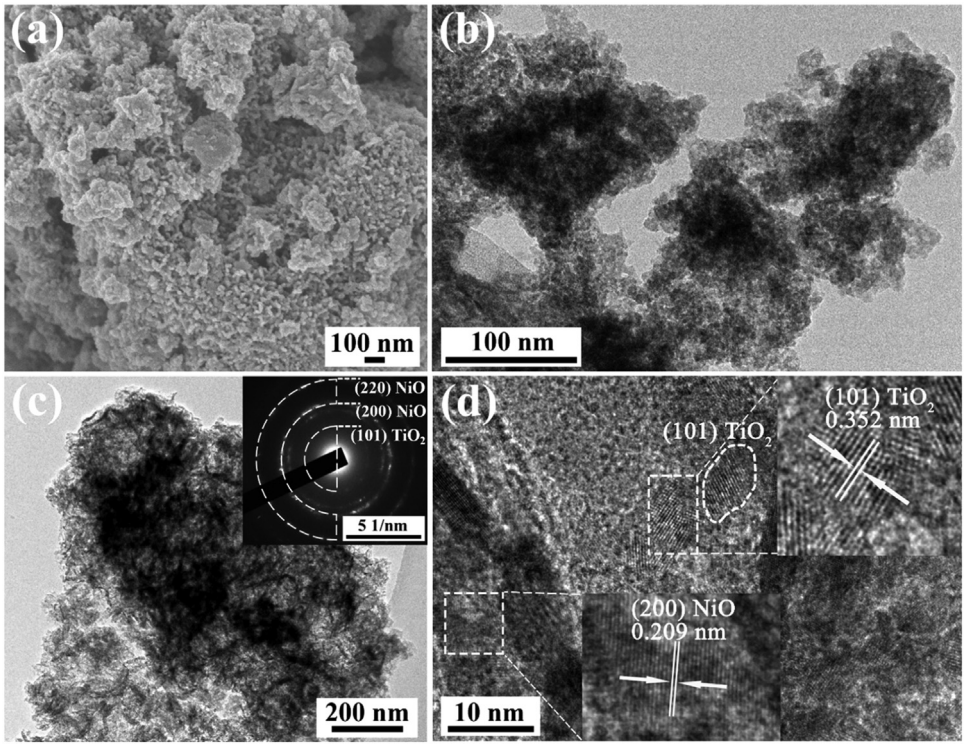

Fig. 8. (a) SEM, (b) TEM and HRTEM images of NiO+TiO_2, and (c) TEM, SAED, and (c) HRTEM images of MMO41.

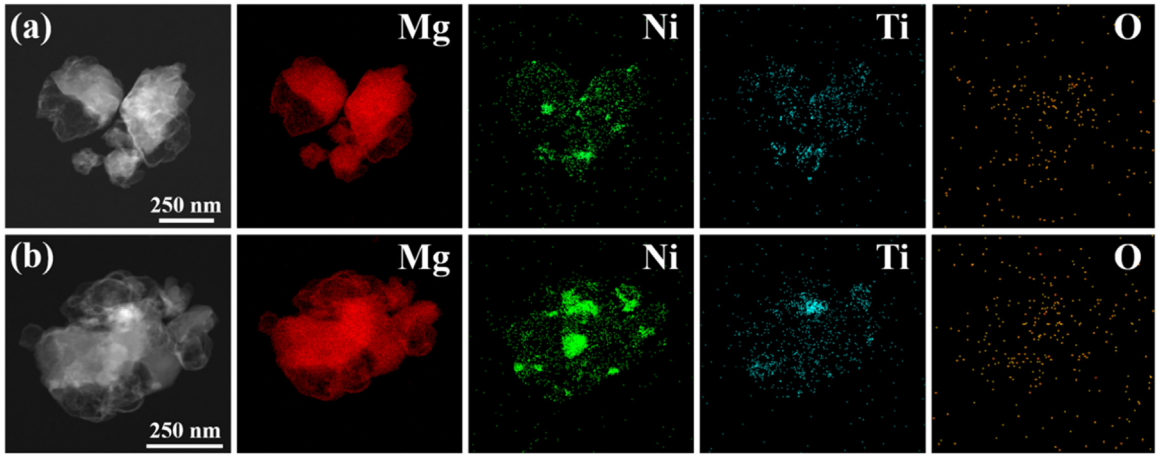

Fig. 9. The EDS mapping of dehydrogenated (a) MgH_2–5%MMO41 and (b) MgH_2–5% (NiO + TiO_2) after activation.

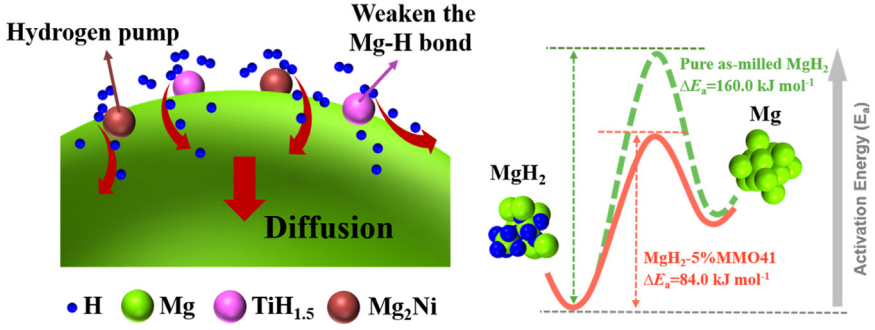

Fig. 10. Schematic illustration of the synergistic effect of the $TiH_{1.5}$−Mg_2Ni nanocatalysts.

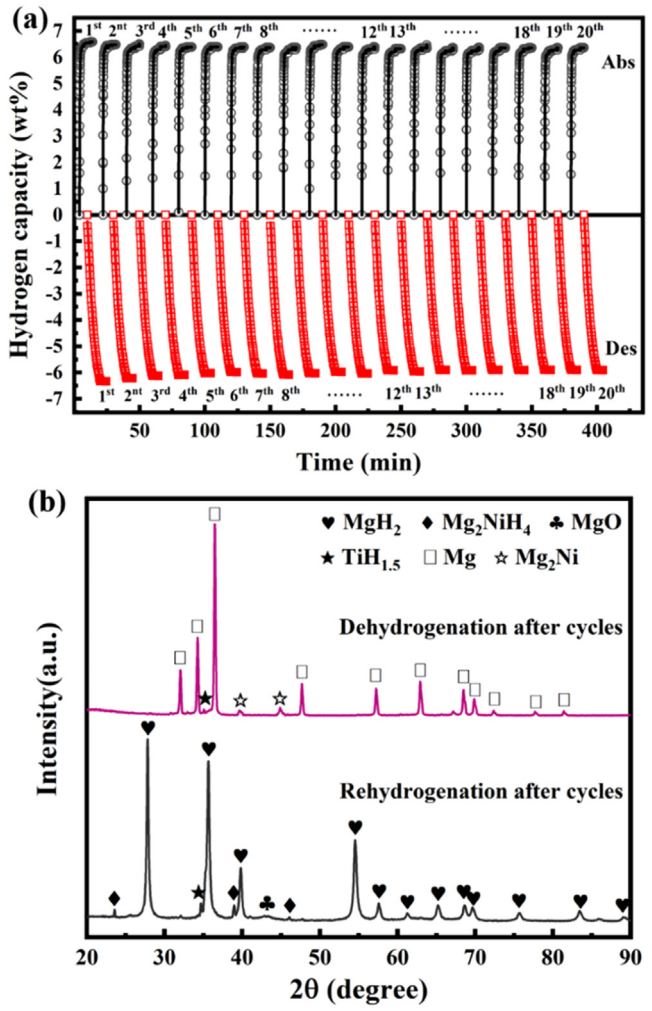

Fig. 11. (a) Cyclic hydrogen storage performance of MgH_2–5%MMO41. (b) XRD patterns of dehydrogenated and hydrogenated samples after 20 cycles.

6.58 wt% in the first cycle to 6.23 wt% in the 20th cycle. The hydrogen desorption capacity decreased from 6.33 wt% in the first cycle to 5.83 wt% in the 20th cycle. The capacity retention rates for cycling hydrogenation and dehydrogenation are 94.7% and 92.1%, respectively, which demonstrate the good cyclic stability of MgH_2–5%MMO41. Furthermore, we tested the XRD patterns of the dehydrogenated and hydrogenated samples after 20 cycles (Fig. 11b). Mg_2Ni (or Mg_2NiH_4) and $TiH_{1.5}$ phases can still be detected after 20 cycles, indicating that the composite catalyst is quite stable during the hydrogen storage process. Similarly, Bhatnagar et al. also reported that TiH_x, as a catalytic active site, can exist stably in hydrogenation-dehydrogenation cycles below 400 °C [68]. And Mg_2Ni can react reversibly with hydrogen ($Mg_2NiH_4 \leftrightarrow Mg_2Ni + 2H_2$) in cyclic hydrogen storage.

4. Conclusions

As a promising solid-state hydrogen storage material and regeneration agent for Li (Na) BH_4, Mg/MgH_2 have attracted considerable attention in hydrogen-energy process chain and hydrogen economics [69–73]. Here, ultrathin Ni/Ti LDH nanosheets with different Ni/Ti ratios were prepared and in-situ converted to Mg_2Ni-$TiH_{1.5}$ composite catalysts to improve the hydrogen storage performance of MgH_2. With the decrease of Ni/Ti ratio from 6:1 to 1:4, the MMO intermediate changes from nanosheets to agglomerated nanoparticles, which results in different compositions and distributions of the final Mg_2Ni-$TiH_{1.5}$ composite catalysts. The catalytic effects of the series of composite catalysts on MgH_2 were discussed in detail. It was found that with the Ni/Ti ratio of 4:1, the Mg_2Ni and $TiH_{1.5}$ nanoparticles generated by MMO reduction have smaller size and more uniform distribution on MgH_2 particle surface, which is more conducive to generating synergistic effects. As a result, the optimal $MgH_2/Mg_2Ni/TiH_{1.5}$ system exhibited significantly improved hydrogen storage performances, i.e. reduced desorption temperature and increased desorption kinetics. This work provides an effective strategy for the preparation of efficient catalysts for Mg/MgH_2 system, and clarifies the mechanism of enhancing the synergistic catalytic effect.

Declaration of competing interest

The authors declare that they have no known competing financial interests or personal relationships that could have appeared to influence the work reported in this paper.

CRediT authorship contribution statement

Gang Huang: Data curation, Formal analysis, Investigation, Methodology, Writing – original draft. **Yao Lu:** Formal analysis, Investigation. **Xiaofang Liu:** Conceptualization, Methodology, Writing – review & editing. **Wukui Tang:** Formal analysis, Investigation. **Xinyu Li:** Data curation, Formal analysis. **Feng Wang:** Data curation, Investigation. **Jianglan Shui:** Methodology, Supervision. **Ronghai Yu:** Resources, Supervision, Validation.

Acknowledgments

This research was supported by National Key Research and Development Program of China (2021YFB4000601), and National Natural Science Foundation of China (51731002, U21A20328).

Supplementary materials

Supplementary material associated with this article can be found, in the online version, at doi:10.1016/j.jma.2023.10.003.

References

[1] P. Jena, J. Phys. Chem. Lett. 2 (2011) 206–211.
[2] K.J. Jeon, H.R. Moon, A.M. Ruminski, B. Jiang, C. Kisielowski, R. Bardhan, J.J. Urban, Nat. Mater. 10 (2011) 286–290.

[3] B. Sakintuna, F. Lamaridarkrim, M. Hirscher, Int. J. Hydrog. Energy 32 (2007) 1121–1140.
[4] G. Huang, X. Liu, Z. Li, Y. Yuan, X. Li, S. Liu, R. Yu, J. Shui, Chem. Eng. J. 473 (2023) 145342.
[5] Y. Yuan, X. Liu, W. Tang, Z. Li, G. Huang, H. Zou, R. Yu, J. Shui, ACS Appl. Mater. Interfaces 15 (2023) 3904–3911.
[6] S. Orimo, Y. Nakamori, J.R. Eliseo, A. Züttel, C.M. Jensen, Chem. Rev. 107 (2007) 4111–4132.
[7] F. Schuth, B. Bogdanovic, M. Felderhoff, Chem. Commun. 20 (2004) 2249–2258.
[8] L. Zaluski, A. Zaluska, J.O. StrÖM-Olsen, J. Alloys Compd. 290 (1999) 71–78.
[9] V. Meregalli, M. Parrinello, Appl. Phys. A Mater. 72 (2001) 143–146.
[10] P. Chen, Science 285 (1999) 91–93.
[11] M.P. Suh, H.J. Park, T.K. Prasad, D.W. Lim, Chem. Rev. 112 (2012) 782–835.
[12] X. Lin, N.R. Champness, M. Schroder, Top. Curr. Chem. 293 (2010) 35–76.
[13] Y.H. Hu, L. Zhang, Adv. Mater. 22 (2010) E117–E130.
[14] K.K. Gangu, S. Maddila, S.B. Mukkamala, S.B. Jonnalagadda, J. Energy Chem. 30 (2019) 132–144.
[15] S. Liu, J. Liu, X. Liu, J. Shang, L. Xu, R. Yu, J. Shui, Nat. Nanotechnol. 16 (2021) 331–336.
[16] S. Liu, J. Liu, X. Liu, J.X. Shang, R. Yu, J. Shui, Appl. Phys. Rev. 9 (2022) 021315.
[17] G.S. Walker, M. Abbas, D.M. Grant, C. Udeh, Chem. Commun. 47 (2011) 8001–8003.
[18] S. Li, X. Yang, J. Hou, W. Du, J. Magnes. Alloys 8 (2020) 78–90.
[19] L. Ouyang, Z. Cao, H. Wang, R. Hu, M. Zhu, J. Alloys Compd. 691 (2017) 422–435.
[20] L.Z. Ouyang, Z.J. Cao, H. Wang, J.W. Liu, D.L. Sun, Q.A. Zhang, M. Zhu, J. Alloys Compd. 586 (2014) 113–117.
[21] L.Z. Ouyang, Z.J. Cao, H. Wang, J.W. Liu, D.L. Sun, Q.A. Zhang, M. Zhu, Int. J. Hydrog. Energy 38 (2013) 8881–8887.
[22] A. Zaluska, L. Zaluski, J.O. StrÖM-Olsen, Appl. Phys. A 72 (2001) 157–165.
[23] A. Pundt, Adv. Eng. Mater. 6 (2004) 11–21.
[24] E.N. Koukaras, A.D. Zdetsis, M.M. Sigalas, J. Am. Chem. Soc. 134 (2012) 15914–15922.
[25] S. Scudino, M. Sakaliyska, K.B. Surreddi, J. Eckert, J. Alloys Compd. 483 (2009) 2–7.
[26] N. Al-Aqeeli, G. Mendoza-Suarez, A. Labrie, R.A.L. Drew, J. Alloys Compd. 400 (2005) 96–99.
[27] N. Hanada, T. Ichikawa, H. Fujii, J. Phys. Chem. B. 109 (2005) 7188–7194.
[28] J.F.R.d. Castro, A.R. Yavari, A. LeMoulec, T.T. Ishikawa, W.J.B. F, J. Alloys Compd. 389 (2005) 270–274.
[29] N.N. Sulaiman, N. Juahir, N.S. Mustafa, F.A. Halim Yap, M. Ismail, J. Energy Chem. 25 (2016) 832–839.
[30] M. Chen, Y. Pu, Z. Li, G. Huang, X. Liu, Y. Lu, W. Tang, L. Xu, S. Liu, R. Yu, J. Shui, Nano Res. 13 (2020) 2063–2071.
[31] L. Zeng, Z. Lan, B. Li, H. Liang, X. Wen, X. Huang, J. Tan, H. Liu, W. Zhou, J. Guo, J. Magnes. Alloys 10 (2022) 3628–3640.
[32] N. Yan, X. Lu, Z. Lu, H. Yu, F. Wu, J. Zheng, X. Wang, L. Zhang, J. Magnes. Alloys 10 (2022) 3542–3552.
[33] J. Song, J. She, D. Chen, F. Pan, J. Magnes. Alloy 8 (2020) 1–41.
[34] A.A. Luo, J. Magnes. Alloy 1 (2013) 2–22.
[35] M.S. Mahmoud, T. Yabe, J. Magnes. Alloy 5 (2017) 430–438.
[36] J. Huot, J.F. Pelletier, L.B. Lurio, M. Sutton, R. Schulz, J. Alloys Compd. 348 (2003) 319–324.
[37] G. Liang, J. Huot, S. Boily, A.V. Neste, R. Schulz, J. Alloys Compd. 291 (1999) 295–299.
[38] J. Cui, J. Liu, H. Wang, L. Ouyang, D. Sun, M. Zhu, X. Yao, J. Mater. Chem. A 2 (2014) 9645–9655.
[39] P.A. Huhn, M. Dornheim, T. Klassen, R. Bormann, J. Alloys Compd. 404-406 (2005) 499–502.
[40] P.M. Jardim, M.O.T. da Conceição, M.C. Brum, D.S. dos Santos, Int. J. Hydrog. Energy. 40 (2015) 17110–17117.
[41] J. Lu, Y.J. Choi, Z.Z. Fang, H.Y. Sohn, E. Roennebro, J. Am. Chem. Soc. 131 (2009) 15843–15852.
[42] H. Imamura, N. Sakasai, Y. Kajii, J. Alloys Compd. 232 (1996) 218–223.
[43] J.L. Bobet, E. Grigorova, M. Khrussanova, M. Khristov, P. Stefanov, P. Peshev, D. Radev, J. Alloys Compd. 366 (2004) 298–302.
[44] M. Zhang, X. Xiao, B. Luo, M. Liu, M. Chen, L. Chen, J. Energy Chem. 46 (2020) 191–198.
[45] M. Au, J. Mater. Sci. 41 (2006) 5976–5980.
[46] S. Deledda, A. Borissova, C. Poinsignon, W.J. Botta, M. Dornheim, T. Klassen, J. Alloys Compd. 404-406 (2005) 409–412.
[47] M.S. Yahya, M. Ismail, J. Energy Chem. 28 (2019) 46–53.
[48] Y. Wang, Q. Zhang, Y. Wang, L. Jiao, H. Yuan, J. Alloys Compd. 645 (2015) S509–S512.
[49] J. Zhang, R. Shi, Y. Zhu, Y. Liu, Y. Zhang, S. Li, L. Li, ACS Appl. Mater. Interfaces 10 (2018) 24975–24980.
[50] M.S. Yahya, M. Ismail, Int. J. Hydrog. Energy 43 (2018) 6244–6255.
[51] J. Chen, G. Xia, Z. Guo, Z. Huang, H. Liu, X. Yu, J. Mater. Chem. A 3 (2015) 15843–15848.
[52] L. Zhang, L. Chen, X. Fan, X. Xiao, J. Zheng, X. Huang, J. Mater. Chem. A 5 (2017) 6178–6185.
[53] L. Zhang, J. Liu, H. Xiao, D. Liu, Y. Qin, H. Wu, H. Li, N. Du, W. Hou, Chem. Eng. J. 250 (2014) 1–5.
[54] C Li, M. Wei, D.G. Evans, X. Duan, Small 10 (2014) 4469–4486.
[55] M. Xu, M. Wei, Adv. Funct. Mater. 28 (2018) 1802943.
[56] Y. Zhao, P. Chen, B. Zhang, D.S. Su, S. Zhang, L. Tian, J. Lu, Z. Li, X. Cao, B. Wang, M. Wei, D.G. Evans, X. Duan, Chem 18 (2012) 11949–11958.
[57] H. Gao, R. Shi, J. Zhu, Y. Liu, Y. Shao, Y. Zhu, J. Zhang, L. Li, X. Hu, Appl. Surf. Sci. 564 (2021) 150302.
[58] P. Yao, Y. Jiang, Y. Liu, C. Wu, K.C. Chou, T. Lyu, Q. Li, J. Magnes. Alloys 8 (2020) 461–471.
[59] G. Liu, Y. Wang, F. Qiu, L. Li, L. Jiao, H. Yuan, J. Mater. Chem. 22 (2012) 22542–22549.
[60] I.E. Malka, M. Pisarek, T. Czujko, J. Bystrzycki, Int. J. Hydrog. Energy 36 (2011) 12909–12917.
[61] D. Pukazhselvan, K.S. Sandhya, D. Ramasamy, A. Shaula, D.P. Fagg, Chem. Phys. Chem. 21 (2020) 1195–1201.
[62] K. Bohmhammel, U. Wolf, G. Wolf, E. Knigsberger, Thermochim. Acta 337 (1999) 195–199.
[63] J.F. Stampfer, C.E. Holley, J.F. Suttle, J. Am. Chem. Soc. 82 (1960) 3504–3508.
[64] W. Zhu, S. Panda, C. Lu, Z. Ma, D. Khan, J. Dong, F. Sun, H. Xu, Q. Zhang, J. Zou, ACS Appl. Mater. Interfaces 12 (2020) 50333–50343.
[65] Q. Kong, H. Zhang, Z. Yuan, J. Liu, L. Li, Y. Fan, G. Fan, B. Liu, ACS Sustain. Chem. Eng. 8 (2020) 4755–4763.
[66] M. Zhang, X. Xiao, J. Mao, Z. Lan, X. Huang, Y. Lu, B. Luo, M. Liu, M. Chen, L. Chen, Mater. Today Energy 12 (2019) 146–154.
[67] J. Cui, H. Wang, J. Liu, L. Ouyang, Q. Zhang, D. Sun, X. Yao, M. Zhu, J. Mater. Chem. A 1 (2013) 5603–5611.
[68] A. Bhatnagar, J.K. Johnson, M.A. Shaz, O.N. Srivastava, J. Phys. Chem. C 122 (2018) 21248–21261.
[69] L. Ouyang, W. Chen, J. Liu, M. Felderhoff, H. Wang, M. Zhu, Adv. Energy Mater. 7 (2017) 1700299.
[70] Y. Shang, C. Pistidda, G. Gizer, T. Klassen, M. Dornheim, J. Magnes. Alloys 9 (2021) 1837–1860.
[71] Q. Li, Y. Lu, Q. Luo, X. Yang, Y. Yang, J. Tan, Z. Dong, J. Dang, J. Li, Y. Chen, B. Jiang, S. Sun, F. Pan, J. Magnes. Alloys 9 (2021) 1922–1941.
[72] Y. Zhu, L. Ouyang, H. Zhong, J. Liu, H. Wang, H. Shao, Z. Huang, M. Zhu, Angew. Chem. Int. Ed. 59 (2020) 8623–8629.
[73] K. Chen, L. Ouyang, H. Zhong, J. Liu, H. Wang, H. Shao, Y. Zhang, M. Zhu, Green Chem. 21 (2019) 4380–4387.